Scintillation resistant wavefront sensing based on multi-aperture phase reconstruction technique

Mathieu Aubailly[1,*] and Mikhail A. Vorontsov[1,2,3]

[1]*Intelligent Optics Laboratory, University of Maryland, 2107 Technology Ventures Building, College Park, Maryland 20740, USA*
[2]*School of Engineering, University of Dayton, 300 College Park, Dayton, Ohio 45469, USA*
[3]*Optonicus, LLC, 711 E. Monument Avenue, Ste 101, Dayton, Ohio 45402, USA*
**Corresponding author: mathieu@umd.edu*

Received January 3, 2012; revised April 6, 2012; accepted June 13, 2012; posted June 13, 2012 (Doc. ID 160765); published July 27, 2012

A scintillation resistant sensor that allows retrieval of an input optical wave phase using a multi-aperture phase reconstruction (MAPR) technique is introduced and analyzed. The MAPR sensor is based on a low-resolution lenslet array in the classical Shack–Hartmann arrangement and two high-resolution photo-arrays for simultaneous measurements of pupil- and focal-plane intensity distributions, which are used for retrieval of the wavefront phase in a two stage process: (a) phase reconstruction inside the sensor pupil subregions corresponding to lenslet subapertures and (b) recovery of subaperture averaged phase components (piston phases). Numerical simulations demonstrate the efficiency of the MAPR technique in conditions of strong intensity scintillations and the presence of wavefront branch points.

OCIS codes: 010.1080, 010.1330, 010.7350, 100.5070.

1. INTRODUCTION

Propagation of optical waves through a medium with random refractive index inhomogeneities such as the Earth's atmosphere may result in strong spatial and temporal fluctuations of wavefront phase and intensity distributions commonly referred to as phase aberrations and intensity scintillations, respectively [1–3]. For near-vertical atmospheric propagation paths—typical for astronomical and space surveillance imaging applications—the turbulence-induced intensity scintillations are relatively weak (weak-scintillation regime [2]) and their impact on system performance is relatively small and quite often can be neglected. Weak-scintillation conditions significantly simplify sensing and mitigation of the turbulence-induced wavefront phase aberrations using adaptive optics (AO) techniques [4]. It comes with no surprise that operational principles of wavefront sensors (WFSs) used in conventional AO systems such as Shack–Hartmann (SH) WFSs [4,5], curvature sensors [6,7], or lateral shearing interferometers [8,9] are based on the assumption of weak scintillations. As experiments and analysis show, these conventional WFSs do not perform well in the conditions of optical wave propagation over near-horizontal or slant atmospheric paths, which are commonly characterized by moderate to strong intensity scintillations. This drawback significantly limits utilization of these wavefront sensing and AO techniques for a number of rapidly growing atmospheric optics applications.

In this paper we introduce and analyze the performance of an optical sensing technique referred to as multi-aperture phase reconstruction (MAPR), which is specifically developed for simultaneous high-resolution sensing of optical field wavefront phase $\varphi(\mathbf{r})$ and intensity $I(\mathbf{r})$ distributions under conditions of strong intensity scintillations. Here $\mathbf{r} = \{x, y\}$ designates a coordinate vector in the MAPR sensor pupil plane. Note that since complex amplitude of an optical field $A(\mathbf{r})$ can be represented in the form $A(\mathbf{r}) = |A(\mathbf{r})| \exp[j\varphi(\mathbf{r})]$, where $|A(\mathbf{r})| = I^{1/2}(\mathbf{r})$, and both phase $\varphi(\mathbf{r})$ and amplitude $|A(\mathbf{r})|$ functions can be obtained from the MAPR sensor measurements, the sensor described can also be considered as a complex field sensor.

In Section 2 we provide a qualitative comparison between the MAPR sensor and the commonly used SH and lens analyzer [Gerchberg–Saxton (GS) technique] sensors and outline both similarities and differences between these wavefront sensing techniques. This section also presents computational steps that are required for phase reconstruction in the MAPR sensor.

Section 3 presents results of the MAPR sensor performance analysis obtained through numerical simulations, and Section 4 concludes this paper by summarizing the results.

2. MAPR SENSOR OPERATIONAL PRINCIPLE

A. MAPR versus Shack–Hartmann and Lens Analyzer (Gerchberg–Saxton) Sensors

The notional schematic of the MAPR sensor is shown in Fig. 1(a). The sensor is composed of an optical reducer, a beam splitter, a lenslet array, and pupil- and focal-plane photo-arrays PA_P and PA_F. The optical reducer and beam splitter are used for reimaging of the sensor pupil onto both the photo-arrays PA_P and lenslet array. The photo-array PA_P provides measurements of the input wave intensity distribution $I^P(\mathbf{r}) = I(M\mathbf{r})$ that is scaled by a factor M by the beam reducer. To simplify notations, we assume $M = 1$ and $I^P(\mathbf{r}) = I(\mathbf{r})$ and only consider a rectangular lenslet array and photo-arrays respectively composed of $N_l = n_l \times n_l$ lenslets and $N_p = n_p \times n_p$ pixels, where n_l and n_p are integers characterizing

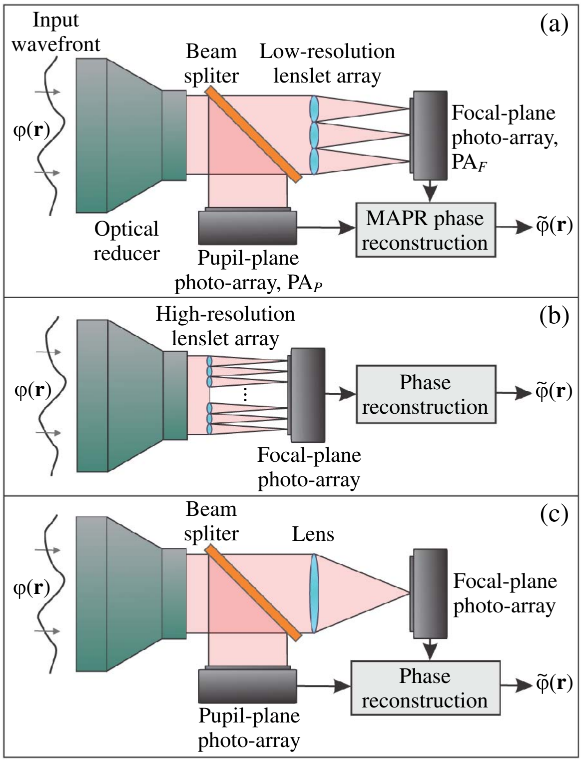

Fig. 1. (Color online) Notional schematics of (a) MAPR, (b) Shack–Hartmann, and (c) lens analyzer wavefront sensors.

lenslet array and photo-array spatial resolutions. The optical assembly composed of the lenslet array and focal-plane photo-array PA_F in Fig. 1(a) is similar to a conventional SH WFS, as shown in Fig. 1(b) [4]. An important difference between these two sensors is that the spatial resolution of the reconstructed phase for the SH sensor is limited by the resolution of the lenslet array, while the resolution for the corresponding MAPR sensor is determined only by the resolution of photo-arrays. Depending on applications, the number of pixels N_p in photo-arrays used in SH sensors usually ranges from $N_p = 128 \times 128$ to $N_p = 512 \times 512$ or sometimes higher, while the number of lenslets N_l seldom exceeds $N_l = 32 \times 32$. In contrast with SH sensors, high-resolution wavefront sensing is achieved in the MAPR sensor using a relatively low-resolution lenslet array. As shown below, the number of lenslets N_l in the MAPR sensor depends on the level of intensity scintillations of the input wave and typically does not exceed $N_l = 4 \times 4$ lenslets even in conditions of strong intensity scintillations.

Another major difference between SH and MAPR sensors is related to the phase reconstruction technique. In SH WFSs phase reconstruction is based on estimating wavefront slopes averaged over lenslet subaperture areas $\{\Omega_l\}$. These wavefront slopes, denoted by vectors $\mathbf{p}_l (l = 1, \ldots, N_l)$, are used for computation of the phase function $\tilde{\varphi}(\mathbf{r})$ within the entire SH sensor aperture. Slope vectors $\{\mathbf{p}_l\}$ are obtained by computing displacements of the lenslet focal spots using subsets $\{I_l^F(\mathbf{r})\}$ of the focal-plane intensity distribution $I^F(\mathbf{r})$. Here the function $I_l^F(\mathbf{r})$ is defined within the lth lenslet subaperture Ω_l and $\mathbf{r} \in \Omega_l$. The subsets $\{I_l^F(\mathbf{r})\}$ of the focal-plane intensity distribution are also used in the MAPR sensor, not for computation of the wavefront slopes, but rather for retrieval of phase functions $\{\tilde{\varphi}_l(\mathbf{r})\}$ $(l = 1, \ldots, N_l)$ inside the subaperture regions $\{\Omega_l\}$. These functions are referred to here as local phases. With the exception of unknown constants $\{\Delta_l\}$ (piston phases), these local phases $\{\tilde{\varphi}_l(\mathbf{r})\}$ represent estimates of the true phase $\varphi(\mathbf{r})$ within their corresponding lenslet subaperture regions $\{\Omega_l\}$, that is, $\varphi_l(\mathbf{r}) = \tilde{\varphi}_l(\mathbf{r}) + \Delta_l$, where $\varphi_l(\mathbf{r})$ is the true phase inside Ω_l. The piston phases $\{\Delta_l\}$ are determined during the second stage of the MAPR phase reconstruction algorithm as described in Subsection 2.C.

Computation of local phases $\{\tilde{\varphi}_l(\mathbf{r})\}$ in the MAPR sensor can be achieved using a well known iterative algorithm such as the GS algorithm [10], the phase diversity algorithm [11], or the conditional gradient descent optimization algorithm [12]. Note that these iterative algorithms were originally developed for phase reconstruction in a WFS commonly referred to as a lens analyzer [12] or phase diversity sensor [13]. A notional schematic of this sensor is shown in Fig. 1(c), which includes a single lens and pupil- and focal-plane photo-arrays. In this sensor, retrieval of the phase function $\varphi(\mathbf{r})$ over the entire sensor aperture is based on iterative processing of the simultaneously captured pupil- and focal-plane intensity distributions, $I^P(\mathbf{r})$ and $I^F(\mathbf{r})$. In contrast, in the MAPR sensor in Fig. 1(a), retrieval of local phases inside the lenslet subaperture regions $\{\Omega_l\}$ is performed using corresponding subsets $\{I_l^P(\mathbf{r})\}$ and $\{I_l^F(\mathbf{r})\}$ of the measured intensity distributions $I^P(\mathbf{r})$ and $I^F(\mathbf{r})$ as described in Subsection 2.B.

In general terms, the MAPR wavefront sensing technique integrates both zonal (aperture division) and modal (phase retrieval over entire aperture) approaches that are utilized correspondingly in the SH and lens analyzer WFS. Similarly to the SH sensor, the input wavefront is subdivided into an array of equally sized zones defined by the lenslet subapertures. At the same time in each zone high-resolution phase retrieval is based on processing of the corresponding pupil- and focal-plane intensity distributions that are dependent on wavefront phase within the entire subaperture—a characteristic of the modal wavefront sensing approach [4]. The final step of phase reconstruction over the entire aperture includes retrieval of piston phases.

Merging both wavefront sensing approaches (zonal and modal) has several advantages. First, note that spatial fluctuations of the input wave intensity and phase inside lenslet subaperture areas are less severe than over the entire sensor aperture. For this reason reconstruction of local phase functions in the MAPR sensor most likely results in faster convergence compared to the corresponding reconstruction over the entire aperture as implemented in the lens analyzer sensor. As shown in Section 3, this results in a more robust phase reconstruction in conditions of strong intensity scintillations compared to both SH and lens analyzer sensors. Another potential advantage of the MAPR sensor is related to computational efficiency. Reconstruction of local phases in the MAPR sensor can be implemented in parallel, i.e., through simultaneous processing of pupil- and focal-plane intensity subsets as illustrated in Fig. 2. This parallel processing can significantly reduce computational time. An additional increase of the phase reconstruction speed can be achieved with a parallel readout of intensity data from the photo-array regions corresponding to lenslet subapertures.

As previously mentioned, the aperture size of individual lenses in the lenslet array of the MAPR sensor is significantly larger than in the SH sensor. This increase of lenslet aperture

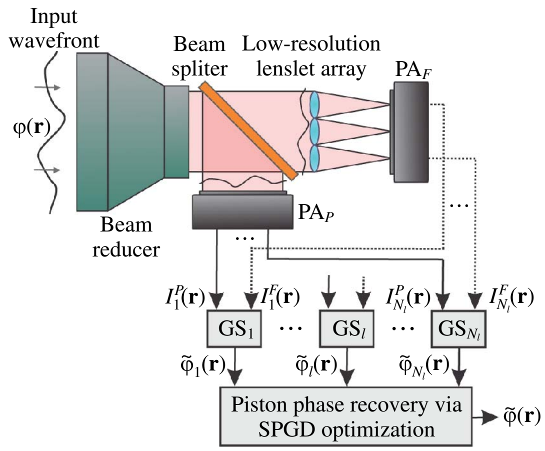

Fig. 2. (Color online) Block diagram of data processing in the MAPR wavefront sensor using parallel computation of local phases $\{\tilde{\varphi}_l(\mathbf{r})\}$ with the Gerchberg–Saxton algorithm (computational blocks $\{\mathrm{GS}_l\}$) and piston phase reconstruction based on stochastic parallel gradient descent (SPGD) optimization techniques.

size without sacrificing spatial resolution in optical phase reconstruction is highly desirable for sensing of phase aberrations that are composed of both large- and small-scale components. The presence of a large-scale phase aberration component may result in significant displacements of the lenslet focal spots. In the case of a conventional SH sensor with relatively small lenslets, this may result in focal spot displacement outside the photo-array regions corresponding to lenslet subapertures causing optical coupling (crosstalk) between neighboring photo-array regions, inaccurate estimation of centroid displacements, and subsequent errors in phase measurements. The use of larger lenslets in the MAPR sensor allows a significant reduction of such crosstalk.

B. Retrieval of Local Phases

As already mentioned, reconstruction of phase $\varphi(\mathbf{r})$ from measured intensity distributions $I^P(\mathbf{r})$ and $I^F(\mathbf{r})$ in the MAPR sensor is performed in two steps: (1) retrieval of local phases $\{\tilde{\varphi}_l(\mathbf{r})\}$ and (2) recovery of piston (subaperture averaged) phases $\{\Delta_l\}$. Several techniques can potentially be applied for computation of local phases from the pupil- and focal-plane subsets, $\{I_l^P(\mathbf{r})\}$ and $\{I_l^F(\mathbf{r})\}$ [10–15]. For simplicity we consider here only the GS algorithm, which represents the most known and widely used phase reconstruction method [10].

Consider briefly the GS iterative procedure for reconstruction of local phase $\tilde{\varphi}_l(\mathbf{r})$ at the lth subaperture. The phase function $\tilde{\varphi}_l(\mathbf{r})$ is obtained by computing a sequence of the corresponding phase functions $\{\tilde{\varphi}_l(\mathbf{r},n)\}$ that presumably converges to $\tilde{\varphi}_l(\mathbf{r}) \cong \varphi_l(\mathbf{r}) + \mathrm{const}$ after a number of iterations N_{it}. Here $n = 0, 1, \ldots, N_{\mathrm{it}}$ and $\tilde{\varphi}_l(\mathbf{r}, 0)$ correspond to the iteration index and an arbitrarily chosen initial phase. Convergence of the iterative process is typically evaluated by calculating a measure (metric) $J_l(n) = J[\tilde{\varphi}_l(\mathbf{r},n)]$ that depends on the reconstructed local phase $\tilde{\varphi}_l(\mathbf{r},n)$ at the nth iteration. Computation of phase $\tilde{\varphi}_l(\mathbf{r},n+1)$ at the $(n+1)$th GS iteration includes the following steps:

(a) Computation of the pupil-plane complex function $A_l^P(\mathbf{r},n) = \sqrt{I_l^P(\mathbf{r})}\exp[i\tilde{\varphi}_l(\mathbf{r},n)]$ using the lth subset of the measured pupil-plane intensity $I_l^P(\mathbf{r})$ and local phase $\tilde{\varphi}_l(\mathbf{r},n)$ obtained at the nth iteration;

(b) Computation of the complex field in the focal plane of the lth lenslet $A_l^F(\mathbf{r},n) = Q[A_l^P(\mathbf{r},n)]$, where Q is the operator describing propagation of an optical wave from the lenslet pupil plane to the focal plane. For an ideal lenslet, Q represents the Fourier transform operator;

(c) Computation of an auxiliary complex function at the lenslet focal plane (focal-plane complex field): $\psi_l^F(\mathbf{r},n) = \sqrt{I_l^F(\mathbf{r})}\exp[i\varphi_l^F(\mathbf{r},n)]$, where $\varphi_l^F(\mathbf{r},n) = \arg[A_l^F(\mathbf{r},n)]$ is the phase of the complex field $A_l^F(\mathbf{r},n)$ and $I_l^F(\mathbf{r})$ is the lth subset of the measured focal-plane intensity;

(d) Computation of an auxiliary complex function at the pupil plane (pupil-plane complex field): $\psi_l^P(\mathbf{r},n) = Q^{-1}[\psi_l^F(\mathbf{r},n)]$, where Q^{-1} is the inverse operator with respect to Q. This operator describes propagation of the optical wave with complex amplitude $\psi_l^F(\mathbf{r},n)$ from the lenslet focal plane to the pupil plane;

(e) Approximation of the local phase at the $(n+1)$th iteration is then given by $\tilde{\varphi}_l(\mathbf{r},n+1) = \arg[\psi_l^P(\mathbf{r},n)]$.

Note that the GS algorithm is equivalent to the conditional gradient descent optimization technique for minimization of the mean-square phase error [12].

The iterative procedure (a) through (e) is repeated a number of iterations N_{it} to ensure convergence of sequence $\{\tilde{\varphi}_l(\mathbf{r},n+1)\}$ toward a small vicinity of the stationary state phase. The number of required iterations N_{it} is commonly defined from the condition $\epsilon(n = N_{\mathrm{it}}) = |[J_l(n) - J_l(n-1)]/J_l(n)| \le \epsilon_0 \ll 1$. The phase function $\tilde{\varphi}_l(\mathbf{r}) \equiv \tilde{\varphi}_l(\mathbf{r}, N_{\mathrm{it}})$ corresponding to the last iteration is considered as an estimate of $\varphi_l(\mathbf{r})$. Note that due to the existence of local minima of the phase error metric $J_l(n)$, the GS iterative process can in principle converge to different phase functions. The probability of the GS process converging to a local minimum increases with the strength of input wave intensity scintillations and phase aberrations. In the strong scintillation regime phase function $\varphi(\mathbf{r})$ can contain phase singularities in the form of branch points (see [16,17]) whose presence significantly reduces convergence speed and most likely results in convergence to a local minimum.

Convergence speed is also highly sensitive to the initial phase functions $\{\tilde{\varphi}_l(\mathbf{r},0)\}$ that the iterative process starts from. The closer $\{\tilde{\varphi}_l(\mathbf{r},0)\}$ is to the true local phases $\{\varphi_l(\mathbf{r})\}$ (up to a constant), the faster the convergence. In the absence of information regarding the true local phases, a set of random functions or constant values can be used as the initial phases $\{\tilde{\varphi}_l(\mathbf{r},0)\}$. In the case of the MAPR sensor, the following more efficient method for setting the initial phase functions $\{\tilde{\varphi}_l(\mathbf{r},0)\}$ can be used. Similar to the conventional SH WFS, one can compute a phase function $\tilde{\varphi}_{\mathrm{SH}}(\mathbf{r})$ over the entire sensor aperture by utilizing the information about focal spot centroid displacements. The initial local phases $\{\tilde{\varphi}_l(\mathbf{r},0)\}$ can then be defined using values of function $\tilde{\varphi}(\mathbf{r},0) = \tilde{\varphi}_{\mathrm{SH}}(\mathbf{r})$ inside the corresponding subaperture areas $\{\Omega_l\}$. Since the GS iterations do not change the subaperture averaged (piston) components of $\{\tilde{\varphi}_l(\mathbf{r},0)\}$, these piston phase values can be calculated and used as the initial piston phases in the iterative process of piston phase reconstruction described in the following section. As shown in Subsection 3.C, this SH sensor-based technique for initial local and piston phase setting allows one to significantly speed up the iteration process of phase reconstruction.

C. Computation of Piston Phases

Consider now the algorithm for retrieval of the piston (subaperture averaged) phases $\{\Delta_l\}$. The general idea is based on the assumption that the lens array is composed of densely packed lenslets, and the local phase functions in the boundary regions between adjacent subapertures are alike.

This assumption can be formulated as a continuity requirement for the true phase function $\varphi(\mathbf{r})$ at the boundary regions between adjacent lenslets. To illustrate, consider three geometries of a densely packed lenslet array, shown in Fig. 3. In the case of lenslets with a circular aperture as shown in Fig. 3(a), the boundary between two adjacent lenslets is reduced to a single point, while in the case of hexagonal and rectangular lenslet shapes as in Figs. 3(b) and 3(c), the corresponding boundary is a line segment. The last two lenslet array geometries are advantageous, since they allow estimation of piston phases based on phase continuity over line segments belonging to adjacent subapertures rather than continuity at a limited number of adjacent points as in Fig. 3(a). This results in significant improvement of accuracy in piston phase retrieval. In the numerical simulations described in Section 3, we consider MAPR sensors with a rectangular lenslet array geometry.

In the lenslet array in Fig. 3(c), consider the set of points $\{\mathbf{r}_{lk}^b\}$ defined as the projection of $\mathbf{r} \in \Omega_l$ onto the boundary line segment (Λ_{lk}) separating the lth subaperture from the adjacent kth subaperture, and introduce the corresponding boundary window function $\rho_{lk}(\mathbf{r}-\mathbf{r}_{lk}^b) = \exp[-|\mathbf{r}-\mathbf{r}_{lk}^b|^2/w^2]$ for $\mathbf{r} \in \Omega_l$ and $\rho_{lk}(\mathbf{r}-\mathbf{r}_{lk}^b) = 0$ otherwise, where w is the boundary width parameter.

Consider the following function (phase continuity metric) that depends on the piston phases

$$J(\Delta_1, \ldots, \Delta_{N_l}) = \sum_{l=1}^{N_l} \epsilon_l^{(0)}(\Delta_1, \ldots, \Delta_{N_l}), \tag{1}$$

where

$$\epsilon_l^{(0)}(\Delta_1, \ldots, \Delta_{N_l}) = \sum_{k\neq l}^{M_l} \left\{ \left[\int_{\Omega_l} \rho_{lk}(\mathbf{r}-\mathbf{r}_{lk}^b)\{\tilde{\varphi}_l(\mathbf{r}) + \Delta_j\} \mathrm{d}^2\mathbf{r} - \int_{\Omega_k} \rho_{kl}(\mathbf{r}-\mathbf{r}_{kl}^b)\{\tilde{\varphi}_k(\mathbf{r}) + \Delta_k\} \mathrm{d}^2\mathbf{r} \right]^2 \right\} \tag{2}$$

is a measure of the phase continuity between the lth subaperture and its M_l neighboring subapertures in the lenslet array. The term $\epsilon_l^{(0)}(\Delta_1, \ldots, \Delta_{N_l})$ evaluates the squared difference integrated over the boundary area (as defined by the window functions $\{\rho_{lk}(\mathbf{r}-\mathbf{r}_{lk}^b)\}$) between the local phase and the corresponding local phase values for all neighboring subapertures. Note that the width of the boundary window function (parameter w) is chosen based on *a priori* information about the characteristic spatial scale of phase inhomogeneities and noise level.

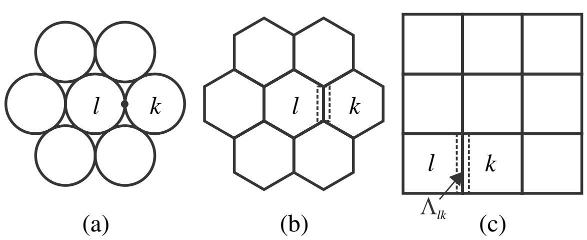

Fig. 3. Examples of densely packed lenslet array configurations for different lenslet shapes: (a) circular, (b) hexagonal, and (c) rectangular. The dot in (a) and dashed rectangles in (b) and (c) indicate the region (Λ_{lk}) used for piston phase reconstruction.

Computation of piston phases in the MAPR sensor is based on minimization of the phase continuity metric [Eq. (1)] as a function of variables $\{\Delta_l\}$. Metric minimization can be performed using the iterative stochastic parallel gradient descent (SPGD) technique [18]. In this technique the desired piston phases $\{\Delta_l\}$ are obtained using the following iterative procedure:

$$\Delta_l^{(n+1)} = \Delta_l^{(n)} + \gamma^{(n)} \delta J^{(n)} \delta\Delta_l^{(n)}, \qquad l = 1, \ldots, N_l, \tag{3}$$

where $\{\Delta_l^{(n)}\}$ are estimates of piston phases at the nth iteration, $\{\delta\Delta_l^{(n)}\}$ and $\{\delta J^{(n)}\}$ are correspondingly small-amplitude random perturbations of piston phases and the metric change resulting from these perturbations, and $\gamma^{(n)}$ is a gain coefficient. The iterative process of the piston phase update [Eq. (3)] is repeated until convergence, and the resulting stationary state values of piston phases $\{\tilde{\Delta}_l\}$ are used to compute wavefront phase $\tilde{\varphi}(\mathbf{r})$ over the entire aperture of the MAPR sensor in the form

$$\tilde{\varphi}(\mathbf{r}) = \sum_{l=1}^{N_l} [\tilde{\varphi}_l(\mathbf{r}) + \tilde{\Delta}_l]. \tag{4}$$

Note that the presence of phase dislocations (branch points) results in 2π phase cuts that may cross boundaries between subapertures. With a relatively small number of branch points (with only a few 2π phase cut lines crossing each boundary region), their impact on the corresponding continuity metric value is relatively small. Nevertheless, an increase of the number of branch points contributes to an overall decrease of the phase reconstruction accuracy that occurs with the increase of intensity scintillation level.

D. Estimation of Computational Efficiency

Consider the computational cost associated with wavefront reconstruction in the MAPR sensor and compare it with the conventional lens analyzer (GS technique). In both sensors, phase reconstruction is performed using digital data processing of the measured intensity distributions $I^P(\mathbf{r})$ and $I^F(\mathbf{r})$. Reconstruction algorithms such as the GS algorithm are based on the calculation of fast Fourier transforms (FFTs). For most implementations of the FFT algorithm, the computational cost is proportional to $N_p \log N_p$, where N_p is the number of data points over the sensor aperture. Correspondingly, the computational cost for phase reconstruction using a lens analyzer/GS sensor is proportional to $C_{\mathrm{LA}} = N_{\mathrm{it}}^{\mathrm{LA}} N_p \log N_p$, where $N_{\mathrm{it}}^{\mathrm{LA}}$ is the number of GS iterations required for phase reconstruction in the lens analyzer/GS. The computational cost of a single local phase reconstruction in the MAPR sensor is proportional to $C_{\mathrm{MAPR}} = N_{\mathrm{it}}^{\mathrm{MAPR}} N_s \log N_s$, where $N_s = N_p/N_l$ is the number of photo-array pixels inside each subaperture of the MAPR sensor and $N_{\mathrm{it}}^{\mathrm{MAPR}}$ is a characteristic number of GS iterations.

Assume that reconstruction of local phases in the MAPR sensor is performed in parallel at each photo-array region corresponding to the lenslet subaperture as illustrated in Fig. 2

(see computational blocks GS_l). In this case we can define a performance factor η that characterizes the ratio of computational cost of phase reconstruction in the lens analyzer/GS versus MAPR sensor:

$$\eta = \frac{C_{\mathrm{LA}}}{C_{\mathrm{MAPR}}} = \frac{N_{\mathrm{it}}^{\mathrm{LA}} N_p \log N_p}{N_{\mathrm{it}}^{\mathrm{MAPR}} N_s \log N_s} = \frac{N_{\mathrm{it}}^{\mathrm{LA}} N_l \log N_p}{N_{\mathrm{it}}^{\mathrm{MAPR}} (\log N_p - \log N_l)} \cong \frac{N_{\mathrm{it}}^{\mathrm{LA}}}{N_{\mathrm{it}}^{\mathrm{MAPR}}} N_l. \quad (5)$$

We assumed here that $N_p \gg N_l$ and also neglected the computational cost related with piston phase retrieval, which does not require Fourier transform computations. For the rectangular lens array with $N_l = n_l \times n_l$, where n_l is the number of lenslets in the array's column or row, from Eq. (5) we obtain

$$\eta \cong \frac{N_{\mathrm{it}}^{\mathrm{LA}}}{N_{\mathrm{it}}^{\mathrm{MAPR}}} n_l^2 = \kappa n_l^2, \quad (6)$$

where $\kappa = N_{\mathrm{it}}^{\mathrm{LA}}/N_{\mathrm{it}}^{\mathrm{MAPR}}$ is the ratio of the number of GS iterations required for phase reconstruction in the lens analyzer/GS and in a single subaperture of the MAPR sensor. Note that the number of GS iterations $N_{\mathrm{it}}^{\mathrm{MAPR}}$ required for phase reconstruction inside the MAPR sensor subaperture is significantly less than the corresponding number of iterations $N_{\mathrm{it}}^{\mathrm{LA}}$ for phase reconstruction inside the entire aperture. Figure 4 shows the performance factor η estimated using desktop personal-computer-based calculations of phase reconstruction for various MAPR lenslet array configurations with n_l ranging from 1 to 7. In the computer simulations we used photo-arrays with $N_p = 512 \times 512$ pixels. As can be seen from Fig. 4, the dependence $\eta(n_l)$ can be quite accurately approximated by the expression in Eq. (6) with $\kappa \approx 17$ (the value for κ was obtained through the best polynomial fit). For example the MAPR phase reconstruction is about 250 times faster in a 4×4 lenslet array configuration than the corresponding phase reconstruction in the lens analyzer/GS sensor.

3. PERFORMANCE ANALYSIS

In this section we present results of the MAPR sensor performance analysis and discuss techniques that can facilitate wavefront reconstruction efficiency.

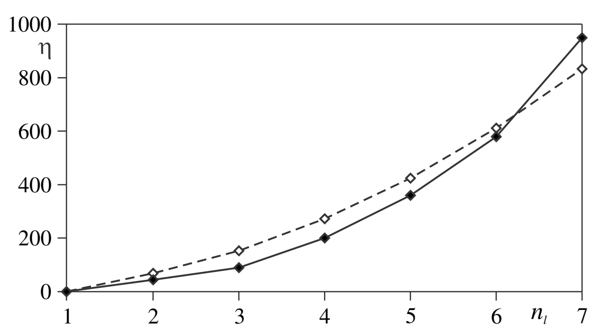

Fig. 4. Performance factor η characterizing the ratio of computational costs for phase reconstruction using the MAPR sensor with the array of $n_l \times n_l$ lenslets and the lens analyzer (GS technique): results of computer simulations (solid curve) and approximation using Eq. (6) with $\kappa = 17$ (dashed curve). The sensor input fields were generated using the technique described in Subsection 3.A.

A. MAPR Sensor Numerical Model

In the analysis of the MAPR sensor performance we used an ensemble of computer-generated random fields as the sensor's input optical waves. Each realization of the input field complex amplitude $A_{\mathrm{in}}(\mathbf{r})$ in the sensor's pupil plane was obtained using the conventional split-operator-based wave-optics simulation of optical beam propagation in a volume atmospheric turbulence [19]. At the beginning of the propagation path at $z = 0$ we used a monochromatic, collimated super-Gaussian beam with complex amplitude $A(\mathbf{r}, z = 0) = A_0 \exp\{-[|\mathbf{r}|^2/(2a_0^2)]^8\}$, where A_0 is the amplitude, $a_0 = D/2$ is the beam width, and D is the MAPR sensor aperture diameter. The optical field complex amplitude at the propagation path end at $z = L$ was utilized as the MAPR sensor input field: $A_{\mathrm{in}}(\mathbf{r}) = A(\mathbf{r}, z = L)$. Optical inhomogeneities along the propagation path were modeled with a set of 10 random thin phase screens corresponding to the Kolmogorov turbulence power spectrum [20]. The phase screens were equally spaced along the propagation path, and their impact (turbulence strength) was characterized by the ratio D/r_0, where r_0 is a characteristic Fried parameter for plane waves [21]. By varying D/r_0 and propagation distance L, one can control the strength of input field phase aberrations and intensity scintillations. In the numerical simulations, D/r_0 ranged from zero

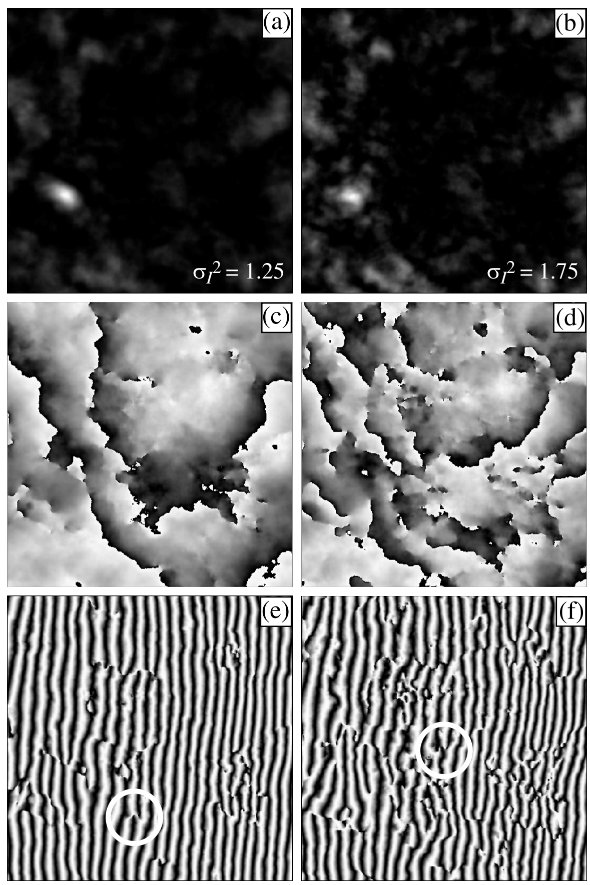

Fig. 5. Gray-scale images corresponding to computer-generated optical field intensity [(a), (b)] and phase [(c), (d)] distributions at the MAPR sensor pupil plane for $D/r_0 = 8$ [(a), (c)] and $D/r_0 = 12$ [(b), (d)]. Phase distributions [(c), (d)] are shown inside a 2π range [between $-\pi$ (black) and $+\pi$ (white)]. (e), (f) The corresponding phase interference patterns. The interference pattern "forks" inside the white circles indicate branch points.

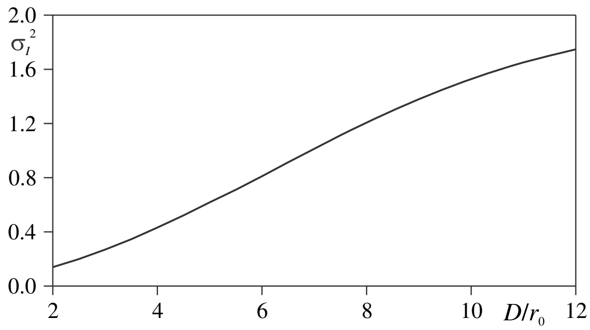

Fig. 6. Aperture averaged scintillation index for the MAPR sensor input fields used in the numerical simulations versus D/r_0 for $L = 0.1L_{\mathrm{dif}}$.

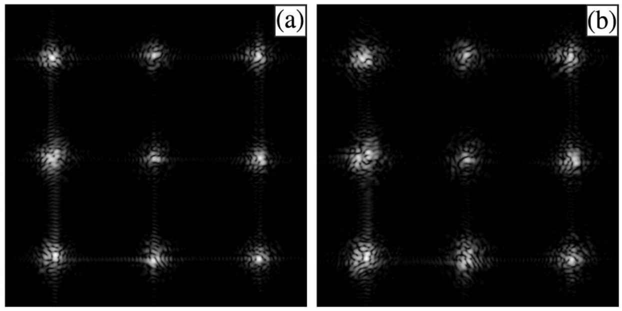

Fig. 7. Intensity distributions in the MAPR sensor lenslet focal plane for input fields shown in Fig. 5: (a) $D/r_0 = 8$ and (b) $D/r_0 = 12$.

(free-space propagation) to 12 and the propagation distance from $L = 0$ (no intensity scintillations) to $L = 0.1L_{\mathrm{dif}}$, where $L_{\mathrm{dif}} = k(D/2)^2$ is the diffractive distance and $k = 2\pi/\lambda$ is the wave number. Figures 5(a)–5(d) show examples of the input field intensity and phase distributions that are obtained using the technique described above. Note that the phase distributions in Figs. 5(c) and 5(d) contain phase discontinuities (branch points) that can be seen as "forks" in the corresponding interference fringes in Figs. 5(e) and 5(f). The interference patterns $I_{\mathrm{INT}}(\mathbf{r})$ in this and other figures are used for qualitative evaluation of the phase reconstruction performance. The interference patterns were computed using the following expression: $I_{\mathrm{INT}}(\mathbf{r}) = 1 + \cos\{\arg[A_{\mathrm{in}}(\mathbf{r})] + \kappa_0 x\}$, where κ_0 is a constant defining spatial frequency of the interference fringes.

The strength of the input field intensity scintillations was characterized by the aperture averaged scintillation index

$$\sigma_I^2 = \frac{1}{S}\int\left\{\frac{\langle[I^P(\mathbf{r})]^2\rangle}{\langle I^P(\mathbf{r})\rangle^2} - 1\right\}\mathrm{d}^2\mathbf{r}, \tag{7}$$

where $I^P(\mathbf{r}) = |A_{\mathrm{in}}(\mathbf{r})|^2$ and S is the MAPR sensor aperture area. Here $\langle\cdot\rangle$ denotes averaging over an ensemble of input fields corresponding to statistically independent realizations of phase screens. In the numerical simulations, 50 sets of phase screens were used for ensemble averaging. Dependence of σ_I^2 on parameter D/r_0 in Fig. 6 shows the range of intensity scintillation used in predictive simulations of the MAPR sensor performance. Change of parameter D/r_0 from zero to $D/r_0 = 12$ allows generation of sensor input fields with a wide range of scintillation index values ($0 \le \sigma_I^2 \le 1.75$).

In the numerical simulations we assumed rectangular lenslet arrays with the number of lenslets in rows and columns ranging from $n_l = 2$ to $n_l = 7$. Each lenslet was represented by a phase mask with a parabolic phase profile $\varphi_l(\mathbf{r}) = k|\mathbf{r} - \mathbf{r}_l|^2/(2F)$, where $\mathbf{r} \in \Omega_l$, $\mathbf{r}_l$ is the coordinate vector corresponding to the lth lenslet center, and F is the focal distance. Note that in practice individual lenslets are separated by narrow gaps. These gaps were modeled by absorbing masks located along the lenslet edges. The mask width was set to 5% of the lenslet size. The intensity distribution in the lenslet focal plane was calculated by considering input wave propagation through the corresponding combined phase and intensity mask with further diffraction over distance F. Figure 7 shows examples of the simulated focal-plane intensity distributions for a 3×3 lens array.

B. Phase Retrieval Accuracy Evaluation

In the numerical simulations of the MAPR sensor we used the GS algorithm for reconstruction of local phases (see Subsection 2.B) and the SPGD-based continuity metric minimization technique described in Subsection 2.C for computation of piston phases. Examples of such simulations are illustrated in Fig. 8. The first stage of MAPR computations resulted in reconstruction of local phases, as shown in Figs. 8(a) and 8(b). The visible sharp boundaries between lenslet regions in the gray-scale images in Figs. 8(a) and 8(b) indicate the existence of errors in piston phases. With retrieval of piston phases at the second step of the MAPR computations, these boundaries nearly vanish [see the corresponding images in Figs. 8(c) and 8(d)].

The accuracy of phase reconstruction can be evaluated with the use of the interference fringe patterns generated for an optical field with uniform intensity and residual phase $\delta(\mathbf{r}) = \varphi(\mathbf{r}) - \tilde{\varphi}(\mathbf{r})$. Consider first the interference patterns in Figs. 8(e) and 8(f), which correspond to reconstructed local phases in Figs. 8(a) and 8(b). Undistorted vertical interference fringes within lenslet regions and discontinuity of these fringes along region boundaries indicate both high quality of local phase reconstruction and the presence of significant errors in piston phases. Retrieval of piston phases resulted in continuity of fringes within the entire sensor aperture, as seen in Figs. 8(g) and 8(h). Note that the piston phases can be reconstructed in parallel with local phases by nesting the SPGD iterative calculations into the GS iterative procedure. This technique of nested GS and SPGD iterative cycles was used in all calculations described. Accuracy of phase reconstruction can also be evaluated using the Strehl ratio that is defined here as [22]

$$\mathrm{St}(n) = \left|\int |A_{\mathrm{in}}(\mathbf{r})|\exp[i\delta(\mathbf{r},n)]\mathrm{d}^2\mathbf{r}\right|^2 // \left[\int |A_{\mathrm{in}}(\mathbf{r})|\mathrm{d}^2\mathbf{r}\right]^2, \tag{8}$$

where $\delta(\mathbf{r},n) = \varphi(\mathbf{r}) - \tilde{\varphi}(\mathbf{r},n)$ is the residual phase obtained after the nth phase reconstruction iteration and $\tilde{\varphi}(\mathbf{r},n)$ is an approximation of the true phase function $\varphi(\mathbf{r})$ by a set of local $\{\tilde{\varphi}_l(\mathbf{r},n)\}$ and piston $\{\Delta_l^{(n)}\}$ phases obtained after the nth iteration. An ideal phase reconstruction corresponds to $\tilde{\varphi}(\mathbf{r}) = \varphi(\mathbf{r}) + \mathrm{const}$ and yields $\mathrm{St} = 1$. The Strehl ratio value in Eq. (8) can also be associated with performance of an adaptive system referred to here as MAPR AO that uses conjugation of the sensor's output phase $\tilde{\varphi}_n(\mathbf{r})$ after each phase reconstruction iteration as an AO wavefront control strategy.

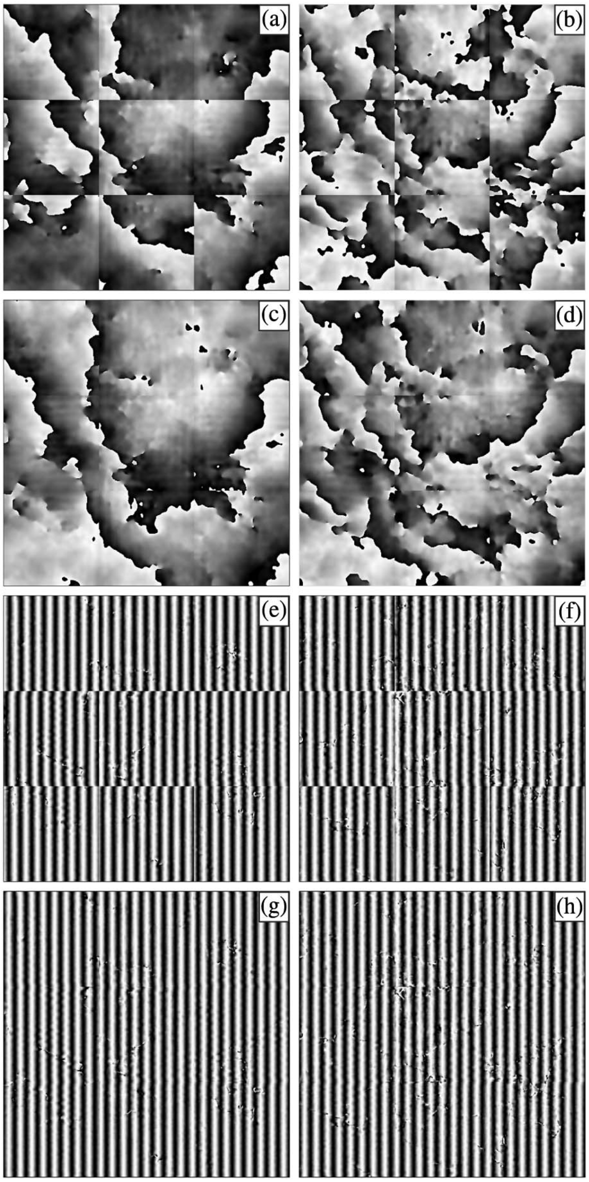

Fig. 8. (a)–(d) Phase distributions and (e)–(h) the corresponding interference patterns obtained after $n = 200$ phase reconstruction iterations using the pupil- and focal-plane intensity distributions from Figs. 5(a) and 5(b) and 7(a) and 7(b). The phase distributions are shown before [(a), (b)] and after [(c), (d)] piston phase recovery. The corresponding interferograms of the residual phase $\varphi(\mathbf{r}) - \tilde{\varphi}(\mathbf{r})$ are shown before [(e), (f)] and after [(g), (h)] piston phase computation.

C. Numerical Analysis of Phase Reconstruction Performance

Compare the efficiency of phase reconstruction with MAPR and lens analyzer/GS sensors using an identical set of computer-generated input field realizations described in Subsection 3.A. This efficiency can be evaluated by considering dependences of the averaged Strehl ratios $\langle \mathrm{St}(n) \rangle$ on the number of the phase reconstruction iterations n. As seen from the corresponding averaged Strehl ratio curves $\langle \mathrm{St}(n) \rangle$ in Fig. 9, reconstruction of phase in the MAPR sensor occurs significantly faster than in the lens analyzer/GS.

The speed of phase reconstruction in the MAPR sensor can be further increased by using the initial conditions

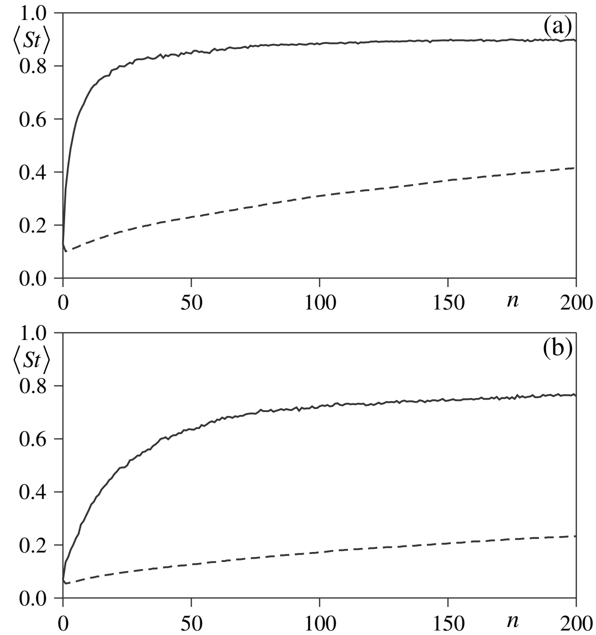

Fig. 9. Phase reconstruction convergence process in the MAPR wavefront sensor with a 3×3 lenslet array (solid curves) and in the lens analyzer/GS sensor (dashed curves) for (a) $D/r_0 = 8$ and (b) $D/r_0 = 12$.

$\{\tilde{\varphi}_l(\mathbf{r}, n = 0)\}$ and $\{\Delta_l^{(n=0)}\}$ discussed in Subsection 2.B. These initial conditions are obtained by considering the combination of the lenslet array and photo-array of the MAPR sensor as a low-resolution SH sensor and correspondingly computing a phase function $\tilde{\varphi}_{\mathrm{SH}}(\mathbf{r})$ with a standard SH phase reconstruction technique. This phase can be utilized to determine $\{\tilde{\varphi}_l(\mathbf{r}, n = 0)\}$ and $\{\Delta_l^{(n=0)}\}$. To illustrate the efficiency of this approach, compare the averaged Strehl ratio evolution curves $\langle \mathrm{St}(n) \rangle$ shown in Fig. 10, obtained using the SH approximation of phase $\tilde{\varphi}_{\mathrm{SH}}(\mathbf{r})$ and spatially uniform and random phase functions as the initial conditions. The results indicate that computation of the initial phase using SH approximation $\tilde{\varphi}_{\mathrm{SH}}(\mathbf{r})$ of the true phase allows significant improvement in phase reconstruction process convergence speed. For this reason the SH-type initial conditions were utilized in all numerical simulations described below. Note that the impact of the initial conditions is significantly less noticeable for the lens analyzer/GS sensor, as indicated in Fig. 10.

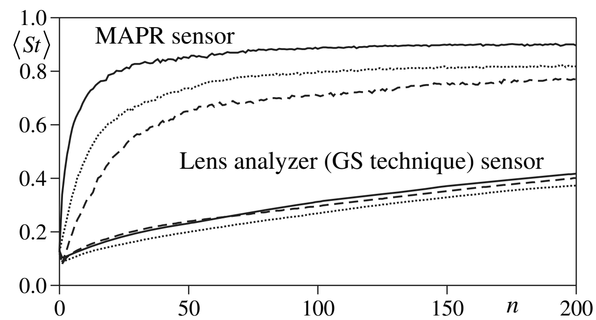

Fig. 10. Averaged Strehl ratio evolution curves for the MAPR (3×3 lenslet array configuration) and lens analyzer/GS sensors with different initial conditions: Shack–Hartmann-based (solid curves), random (dashed curves), and spatially uniform (dotted curves) initial phase functions. The sensor input field realizations correspond to $D/r_0 = 8$.

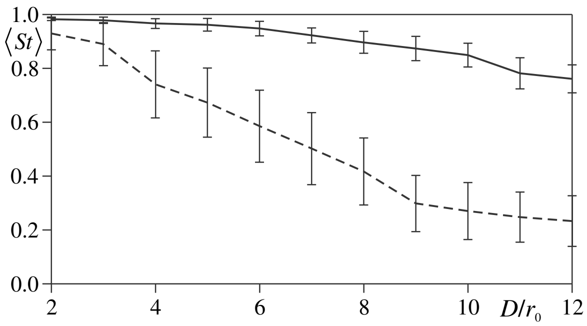

Fig. 11. Performance curves (Strehl ratios versus D/r_0) for the MAPR 3×3 lenslet array (solid curve) and lens analyzer/GS (dashed curve) sensors. The length of the vertical lines indicates the standard deviation obtained for the corresponding Strehl ratio value.

Consider now performance of the MAPR and lens analyzer/GS sensors in operation with input optical waves that encounter a different level of atmospheric-turbulence-induced phase aberrations and intensity scintillations, which is characterized by the D/r_0 ratio. In the numerical simulations for each D/r_0 value a set of 50 statistically independent input fields were generated using the technique described in Subsection 3.A. For each input field realization we performed 200 iteration of phase reconstruction calculations and computed Strehl ratios corresponding to the residual phases. The dependence of the averaged Strehl ratio $\langle \mathrm{St}(n = 200) \rangle$ on D/r_0 is shown in Fig. 11 for both MAPR and lens analyzer/GS sensors. As seen from the presented results, the MAPR sensor can provide high-quality phase reconstruction that is characterized by the averaged Strehl ratio exceeding 0.9 for input fields with $D/r_0 \leq 8$ and the scintillation index σ_I^2 ranging from zero to $\sigma_I^2 = 1.25$. Residual phase Strehl ratio values that exceed 0.8 can be achieved with input fields with $0 \leq D/r_0 \leq 12$ and scintillation index $0 \leq \sigma_I^2 \leq 1.75$. These results clearly demonstrate the robustness of the MAPR sensor with respect to input field intensity scintillations and the presence of phase branch points, which is significantly higher if compared with both the SH and lens analyzer/GS sensors. The SH sensor appeared to be the most sensitive to the input field intensity scintillations. The corresponding computer simulations of the SH sensor with a 16×16 lenslet array resulted in significant errors in phase reconstruction when the scintillation index exceeded 0.3.

Note that there are several factors limiting the Strehl ratio in the presented results. First, in order to perform a fair comparison between the MAPR and the lens analyzer/GS techniques, we performed a fixed number of phase reconstruction iterations (200 iterations) for both approaches. The Strehl ratio for both techniques can be improved by increasing the number of iterations. However, Fig. 9 shows how the MAPR reconstruction converges significantly faster than the GS approach. Another factor limiting the Strehl ratio under strong scintillation is that reconstruction is more likely to get trapped in local extrema and stagnate as the complexity of the phase increases. It should be emphasized, however, that reconstruction over subapertures (less data points) reduces the likelihood of stagnation compared to reconstruction over the entire aperture as in the GS technique. Finally, cross talk between subapertures in the MAPR sensor reduces the accuracy of the reconstruction, as discussed later in this section.

Robustness of the MAPR sensor operation with respect to intensity scintillations and phase reconstruction speed depends on the lenslet array resolution. In the case of rectangular arrays with $n_l \times n_l$ lenslets, the lenslet array resolution is defined by the number n_l of lenslets in the array's rows and columns. In the numerical simulations we examined operation of MAPR sensors with different resolutions of lenslet arrays (n_l ranging from 2 to 7) using identical sets of input optical fields corresponding to weak ($D/r_0 = 4$), medium ($D/r_0 = 8$), and strong ($D/r_0 = 12$) turbulence conditions. The calculated dependence of the averaged Strehl ratio $\langle \mathrm{St} \rangle$ of the residual phase after 200 iterations of phase reconstruction on lenslet array resolution n_l is shown in Fig. 12 for input fields with different D/r_0 parameters.

The presented results show that performance of the MAPR sensor in terms of the Strehl ratio achieves an optimal value for lenslet array configurations with n_l ranging between $n_l = 3$ and $n_l = 5$. In general, the optimum lenslet array configuration depends on the right balance between two contradictory factors: while an increase of lenslet array resolution (decrease of lenslet aperture size) is desired, as it leads to faster phase reconstruction convergence, it also eventually results in an undesired increase of cross talk between focal-plane intensity distributions and errors in phase reconstruction (see corresponding discussions in Subsections 2.A and 2.D). The optimal balance of these factors and, hence, optimal lenslet array configuration depend on the strength of the turbulence that impacted the sensor's input field. In conditions of weak turbulence, the optimal performance is achieved with a higher resolution lenslet array, since in weak turbulence conditions phase aberrations are relatively small and one can decrease the lenslet aperture size while avoiding potential cross talk between focal spots that belongs to neighboring lenslet array subapertures. As shown in Fig. 12, in strong turbulence conditions the optimal MAPR sensor performance is achieved with a lower resolution lenslet array: $n_l = 4$ for $D/r_0 = 12$ versus $n_l = 5$ for $D/r_0 = 8$. The increase of lenslet subaperture is related to turbulence-induced focal spot widening, leading to an increase of the cross talk. Note that the results presented in Fig. 12 are obtained using a fixed number of phase reconstruction iterations for MAPR sensors with different resolutions of lenslet arrays and thus do not account for a computational performance increase that can be achieved using parallel computations as discussed in Subsection 2.D.

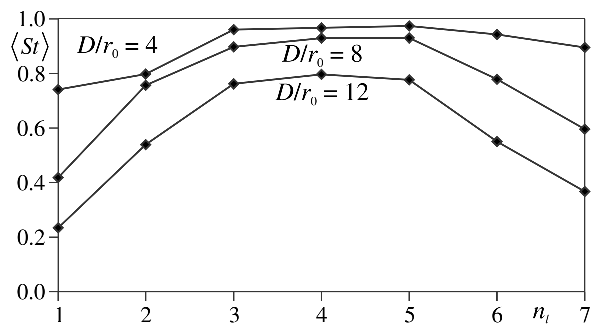

Fig. 12. Averaged Strehl ratio for the residual phase achieved after 200 MAPR phase reconstruction iterations versus number of lenslets n_l in rows and columns of a rectangular lenslet array for $D/r_0 = 4$, 8, and 12.

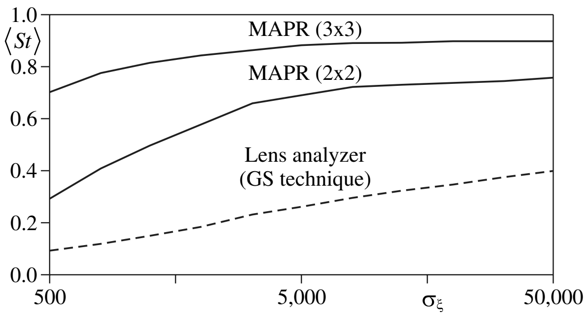

Fig. 13. Averaged Strehl ratios versus photo-array noise parameter σ_ξ for the MAPR sensor with 3×3 and 2×2 lenslet arrays (solid curves) and lens analyzer/GS sensor (dashed curve) for input fields with $D/r_0 = 8$.

D. Impact of Photo-Sensor Noise

Consider now wavefront sensing conditions that are characterized by a relatively low level of input field photon flux. These operational conditions require consideration of a noise signal that is superimposed with intensity distributions of both MAPR sensor photo-arrays. In the numerical simulations this noise was represented by delta-correlated random fields with Gaussian probability distribution, zero mean, and standard deviation σ. The standard deviation value σ can be associated with the strength of the photon noise at photo-array pixels. For each realization of the input field, the noise signal strength can be characterized by factors $\xi^P = I^P_{\max}/\sigma$ and $\xi^F = I^F_{\max}/\sigma$, where $I^P_{\max}$ and $I^F_{\max}$ are maximum values of the MAPR sensor pupil- and focal-plane intensity distributions $I^P(\mathbf{r})$ and $I^F(\mathbf{r})$. The factors ξ^P and ξ^F also characterize the dynamical range of the WFS, defined as the ratio of maximum number of photons received by a sensor's photo-array pixel to the number of noise photons per pixel.

In the numerical simulations we assumed that the average noise factors are identical for both pupil- and focal-plane photo-arrays $\langle\xi^F\rangle = \langle\xi^P\rangle = \langle\xi\rangle$, which can be achieved by adjusting the input field optical power entering the photo-arrays. In the simulations we used an identical set of 50 field realizations corresponding to atmospheric turbulence conditions with $D/r_0 = 8$ as the input fields for both the MAPR and lens analyzer/GS sensors. Prior to phase reconstruction calculations we superimposed a delta-correlated noise pattern with a fixed σ into both pupil- and focal-plane intensity distributions. The obtained "noisy" intensity patterns were used for phase reconstruction. The residual phase achieved after 200 iterations of phase reconstruction calculations was used for computation of the Strehl ratio St and factors ξ^P and ξ^F. The Strehl ratio values obtained for different input field and noise realizations were averaged. The computations were repeated using the same set of input fields with a superimposed noise pattern having different standard deviation σ. The obtained dependence of the averaged Strehl ratio $\langle\mathrm{St}\rangle$ on the averaged noise factor standard deviation $\sigma_\xi = \sqrt{\langle\xi^2\rangle}$ is presented in Fig. 13. The results show that photo-array noise can significantly impact phase reconstruction performance of both MAPR and lens analyzer/GS sensors. Nevertheless the MAPR sensor is significantly less sensitive to photo-array noise. In Fig. 13 the averaged Strehl ratio achieved with the MAPR sensor remains at least twice larger than the lens analyzer/GS for the entire range of noise factors examined. For the MAPR sensor with a 3×3 lenslet array, the impact of photo-array noise on phase reconstruction accuracy can be practically neglected when the maximum value of received photon flux exceeds the corresponding noise level by a factor of $\xi = 1,000$. Note that the results in Fig. 13 also reveal a strong dependence of the MAPR sensor performance with respect to the lenslet array resolution (compare performance of the MAPR sensors having photo-arrays with 2×2 and 3×3 lenslets).

4. CONCLUSION

We introduced and analyzed the performance of a new WFS referred to as multi-aperture phase reconstruction (MAPR) sensor. This sensor is specifically developed for simultaneous high-resolution sensing of optical field wavefront phase under conditions of strong intensity scintillations. This sensor merges the SH and the lens analyzer/GS wavefront sensing paradigms by integrating both zonal (aperture division) and modal (phase retrieval over entire aperture) approaches. The input wavefront is subdivided into equally sized zones defined by low-resolution lenslet subapertures. In each zone high-resolution phase retrieval is based on an iterative processing of the corresponding subsets of the pupil- and focal-plane intensity distributions that are similar to the lens analyzer wavefront sensing technique. The final step of phase reconstruction over the entire aperture includes retrieval of piston phases based on minimization of the introduced continuity metric. It is shown that due to the parallel nature of the optical and signal processing, the MAPR sensor can provide significantly faster phase reconstruction and can operate robustly even in conditions of strong intensity scintillations.

ACKNOWLEDGMENTS

The authors want to thank Svetlana Lachinova for the helpful discussions.

REFERENCES

1. V. U. Zavorotnyi, "Strong fluctuations of the wave intensity behind a randomly inhomogeneous layer," Radiophys. Quantum Electron. **22**, 352–354 (1979).
2. M. C. Rytov, Yu A. Kravtsov, and V. I. Tatarskii, eds., *Principles of Statistical Radiophysics 4*, *Wave Propagation Through Random Media* (Springer-Verlag, 1989).
3. L. C. Andrews, R. L. Phillips, C. Y. Hopen, and M. A. Al-Habash, "Theory of optical scintillation," J. Opt. Soc. Am. A **16**, 1417–1429 (1999).
4. J. W. Hardy, *Adaptive Optics for Astronomical Telescopes* (Oxford University, 1998).
5. J. D. Barchers, D. L. Fried, and D. J. Link, "Evaluation of the performance of Hartmann sensors in strong scintillation," Appl. Opt. **41**, 1012–1021 (2002).
6. F. Roddier, "Curvature sensing and compensation: a new concept in adaptive optics," Appl. Opt. **27**, 1223–1225 (1988).
7. G. Rousset, "Wave-front sensors," in *Adaptive Optics in Astronomy*, F. Roddier, ed. (Cambridge University, 1999), pp. 91–130.
8. J. W. Hardy, J. E. Lefebvre, and C. L. Koliopoulos, "Real-time atmospheric compensation," J. Opt. Soc. Am. **67**, 360–369 (1977).
9. D. G. Sandler, L. Cuellar, M. Lefebvre, T. Barrett, R. Arnold, P. Johnson, A. Rego, G. Smith, G. Taylor, and B. Spivey, "Shearing interferometry for laser-guide-star atmospheric correction at large D/r_0," J. Opt. Soc. Am. **11**, 858–873 (1994).
10. R. W. Gerchberg and W. O. Saxton, "A practical algorithm for the determination of phase from image and diffraction plane pictures," Optik **35**, 237–246 (1972).
11. R. A. Gonsalves, "Phase retrieval from modulus data," J. Opt. Soc. Am. **66**, 961–964 (1976).

12. V. Y. Ivanov, V. P. Sivokon, and M. A. Vorontsov, “Phase retrieval from a set of intensity measurements: theory and experiment,” J. Opt. Soc. Am. **9**, 1515–1524 (1992).
13. R. G. Paxman and J. R. Fienup, “Optical misalignment sensing and image reconstruction using phase diversity,” J. Opt. Soc. Am. A **5**, 914–923 (1988).
14. J. R. Fienup, “Phase retrieval algorithms: a comparison,” Appl. Opt. **21**, 2758–2769 (1982).
15. J. R. Fienup and C. C. Wackerman, “Phase-retrieval stagnation problems and solutions,” J. Opt. Soc. Am. A **3**, 1897–1907 (1986).
16. D. L. Fried, “Branch point problem in adaptive optics,” J. Opt. Soc. Am. A **15**, 2759–2768 (1998).
17. D. L. Fried and J. L. Vaughn, “Branch cuts in the phase function,” Appl. Opt. **31**, 2865–2882 (1992).
18. M. A. Vorontsov and V. P. Sivokon, “Stochastic parallel-gradient-descent technique for high-resolution wave-front phase-distortion correction,” J. Opt. Soc. Am. A **15**, 2745–2758 (1998).
19. J. A. Fleck, J. R. Morris, and M. D. Feit, “Time-dependent propagation of high energy laser beams through the atmosphere,” Appl. Phys. **10**, 129–160 (1976).
20. M. C. Roggemann and B. Welsh, *Imaging Through Turbulence* (CRC, 1996).
21. D. L. Fried, “Anisoplanatism in adaptive optics,” J. Opt. Soc. Am. **72**, 52–61 (1982).
22. E. W. Justh, M. A. Vorontsov, G. W. Carhart, L. A. Beresnev, and P. S. Krishnaprasad, “Adaptive optics with advanced phase-contrast techniques. II. high-resolution wave-front control,” J. Opt. Soc. Am. A **18**, 1300–1311 (2001).